

Measurement of the T_{CMB} evolution from the Sunyaev-Zel'dovich effect

G. Hurier¹, N. Aghanim¹, M. Douspis¹, and E. Pointecouteau^{2,3}

¹ Institut d'Astrophysique Spatiale, CNRS (UMR8617) Université Paris-Sud 11, Bâtiment 121, 91405 Orsay Cedex, France
e-mail: ghurier@ias.u-psud.fr

² CNRS, IRAP, 9 Av. colonel Roche, BP 44346, 31028 Toulouse Cedex 4, France

³ Université de Toulouse, UPS-OMP, IRAP, 31400 Toulouse, France

Received 9 September 2013 / Accepted 27 November 2013

ABSTRACT

In the standard hot cosmological model, the black-body temperature of the cosmic microwave background (CMB), T_{CMB} , increases linearly with redshift. Across the line of sight CMB photons interact with the hot ($\sim 10^7\text{--}8$ K) and diffuse gas of electrons from galaxy clusters. This interaction leads to the well-known thermal Sunyaev-Zel'dovich effect (tSZ), which produces a distortion of the black-body emission law, depending on T_{CMB} . Using tSZ data from the *Planck* satellite, it is possible to constrain T_{CMB} below $z = 1$. Focusing on the redshift dependence of T_{CMB} , we obtain $T_{\text{CMB}}(z) = (2.726 \pm 0.001) \times (1+z)^{1-\beta}$ K with $\beta = 0.009 \pm 0.017$, which improves on previous constraints. Combined with measurements of molecular species absorptions, we derive $\beta = 0.006 \pm 0.013$. These constraints are consistent with the standard (i.e. adiabatic, $\beta = 0$) Big-Bang model.

Key words. cosmology: observations – cosmic background radiation – galaxies: clusters: general

1. Introduction

The cosmic microwave background (CMB) radiation is a fundamental observational probe of the hot Big-Bang model. In standard Λ CDM cosmology, the CMB black-body temperature evolution as a function of redshift reads $T_{\text{CMB}}(z) = T_{\text{CMB}}(z=0)(1+z)^{1-\beta}$, with $\beta = 0$ and $T_{\text{CMB}}(z=0)$ is the temperature measured today in the local Universe.

A violation of this evolution would imply deeper theoretical consequences (e.g., Uzan et al. 2004). Alternative cosmological models predict a nonlinear scaling law between temperature and redshift (see e.g., Matyjasek 1995; Overduin & Cooperstock 1998; Puy 2004). A deviation from $\beta = 0$ can be induced by a violation of the equivalence principle or by a non-conservation of the photon number without any spectral distortion of the CMB. In the first case, it can be associated with fundamental constant variations (see e.g., Murphy et al. 2003; Srianand et al. 2004). In the second case, it can be associated with decaying dark-energy models (see e.g., Freese et al. 1987; Lima & Trodden 1996; Jetzer et al. 2011) or with axion-photon-like coupling process (see Jaeckel & Ringwald 2010, for a recent review).

The CMB temperature has been measured in our galaxy at high precision using CN excitation in molecular clouds by Roth et al. (1993). Next, it has been measured using the COBE-FIRAS experiment (Fixsen et al. 1996; Mather et al. 1999) and more recently, using the WMAP data (Bennett et al. 2003) to recalibrate the COBE-FIRAS (Fixsen 2009) measurements.

In addition to the measurement of T_{CMB} at $z = 0$, there are currently two direct observational methods to measure T_{CMB} at redshifts $z > 0$. The first one uses the excitation of interstellar atomic or molecular species by CMB photons (e.g. Losecco et al. 2001). This approach was used even before the CMB discovery (see Thaddeus 1972, for a review of early observations). When in radiative equilibrium with the CMB radiation,

the excitation temperature of molecular species equals that of the CMB. Thus, these species allow one to measure the CMB temperature (Bahcall & Wolf 1968). The fact that the CMB is not the only heating source of the interstellar medium and the lack of a detailed knowledge of the physical conditions in the absorbing clouds are the main sources of systematics and uncertainties (Combes & Wiklind 1999). They lead to upper limits or large error bars ($\Delta T \geq 0.6$ K) on the value of T_{CMB} (Meyer et al. 1986; Songaila et al. 1994a,b; Lu et al. 1996; Roth & Bauer 1999). Recently, Muller et al. (2013) have performed a comprehensive analysis that overcomes parts of the limitations. In particular, they have made use of various atomic and molecular species simultaneously in order to completely model the observed cloud properties and hence to provide tight constraints on T_{CMB} .

The second observational approach consists in measuring a weak spectral distortion of the CMB black-body in the direction of galaxy clusters that is caused by the thermal Sunyaev-Zel'dovich (tSZ) effect (Zel'dovich & Sunyaev 1969; Sunyaev & Zel'dovich 1972). This technique was originally proposed by Fabbri et al. (1978) and Rephaeli (1980). Predictions for these measurement with *Planck* have been discussed by Horellou et al. (2005) and de Martino et al. (2012). They predicted, in an optimistic case, an uncertainty on the T_{CMB} evolution of $\Delta\beta \sim 0.011$. Actual measurements were already performed (Battistelli et al. 2002; Luzzi et al. 2009) and provided $\Delta T \leq 0.3$ K on a small number of clusters of galaxies. The *Planck* satellite now offers a new and large sample of galaxy clusters (Planck Collaboration 2014i) observed via the tSZ effect that allows us to derive much tighter constraints on the evolution of the CMB temperature.

Galaxy cluster catalogs that reach deeper (e.g. SPT, Reichardt et al. 2013 and ACT, Hasselfield et al. 2013) or larger (e.g. MCXC, Piffaretti et al. 2011) can also be used to complement the constraint from the *Planck* SZ clusters.

In this work, we focus on improving in the measurement of T_{CMB} at redshifts $z > 0$ from the *Planck* data using the tSZ effect from galaxy clusters. In Sect. 2 we present the *Planck* intensity maps and galaxy cluster catalog that were used. Sect. 3 briefly presents the tSZ effect. Then in Sect. 4, we present the stacking method used to extract the tSZ flux in the different *Planck* frequency channels to constrain T_{CMB} . In Sect. 5, we estimate the uncertainty levels on our measurement that are caused, on the one hand, by foreground/background contributions to *Planck* intensity maps and, on the other hand, by instrumental systematic effects. Next in Sect. 6, we carefully model our measurement to determine T_{CMB} from the tSZ spectral law. In Sect. 7, we present our results and compare them with previous measurements. Finally in Sect. 8, we discuss our results and their cosmological implications.

2. Data

2.1. *Planck* intensity maps

We used the six channel maps, 100 to 857 GHz, from the *Planck* satellite (Planck Collaboration 2014a). We refer to the Planck Collaboration (2014c) and Planck Collaboration (2014e) for the generic scheme of time ordered information processing and map-making, as well as for the characteristics of the *Planck* frequency maps. We used the *Planck* channel maps in HEALPix (Górski et al. 2005) $N_{\text{side}} = 2048$ at full resolution. Here, we approximate the *Planck* beams by effective circular Gaussians (see Planck Collaboration 2014d, for more details).

2.2. *Planck* SZ catalog

We also used the *Planck* catalog of tSZ detections (Planck Collaboration 2014i, PSZ). It contains 1227 sources, which is about six times larger than the *Planck* Early SZ (ESZ; Planck Collaboration 2011a) sample and is currently the largest tSZ-selected catalog. The PSZ contains 861 confirmed clusters to date.

In the following, we only consider the sample of 813 *Planck* cluster with redshifts up to ~ 1 (Planck Collaboration 2011d). This sample consists of high-significance SZ detections in the *Planck* channel maps and thus allows us to constrain T_{CMB} up to $z \sim 1$, avoiding strong contamination by point sources or galactic emission.

2.3. Other catalogs of galaxy clusters

We complemented our analysis of the *Planck* SZ-cluster catalog using X-ray selected clusters from the Meta Catalog of X-ray Clusters (MCXC; Piffaretti et al. 2011); and tSZ selected clusters from the Atacama Cosmological Telescope (ACT; Hincks et al. 2010; Hasselfield et al. 2013) and the South Pole Telescope (SPT) tSZ catalogs (Chang et al. 2009; Song et al. 2012; Reichardt et al. 2013). Table 1 summarizes the main characteristics of these catalogs. In particular, for the present study, we considered subsamples from the MCXC, ACT, and SPT catalogs that consist of clusters not included in the PSZ catalog; for the MCXC clusters we also imposed that $M_{500} \geq 10^{14} M_{\odot}$.

2.4. Radio-source catalogs

Emission from radio point sources is a source of contamination in the estimation of the tSZ flux (Planck Collaboration 2014i) that can lead to biases in tSZ Compton- y signal (see e.g.

Table 1. Main characteristics of the galaxy cluster catalogs.

Catalog	N_{cl}	N_{cl}^*	\bar{z}	z_{med}	σ_z	f_{sky}
<i>Planck</i> SZ	1227	813	0.247	0.220	0.159	0.84
MCXC	1743	823	0.222	0.166	0.172	— ¹
SPT	224	142	0.574	0.576	0.279	0.02
ACT	91	61	0.586	0.570	0.267	0.01

Notes. N_{cl} is the number of objects in the catalog, N_{cl}^* is the number of clusters in the present work, \bar{z} is the mean redshift, z_{med} is the median redshift, σ_z is the redshift dispersion of the catalog, and f_{sky} is the sky coverage of the catalog. ⁽¹⁾ The MCXC is a meta-catalog based on ROSAT All Sky Survey catalogs (see Piffaretti et al. 2011, and reference therein).

Hurier et al. 2013, for an example on the Virgo and Perseus galaxy clusters).

The NRAO VLA Sky Survey (NVSS; Condon et al. 1998) is a 1.4 GHz continuum survey covering the entire sky north of Dec $> -40^\circ$. The associated catalog of discrete sources contains over 1.8 million radio sources. South of Dec $< -30^\circ$ and at galactic latitudes $|b| > 10^\circ$, the Sydney University Molonglo Sky Survey (SUMSS; Mauch et al. 2003, 2008) is a 843 MHz continuum survey also providing a radio source catalog. SUMSS and NVSS have a similar sensitivity and angular resolutions, and combined they cover the whole sky.

We used these two surveys as tracers of the radio emission that contaminated our estimation of the tSZ flux to estimate the level of bias in our measure.

3. The tSZ effect

The tSZ effect is a distortion of the CMB black-body radiation through inverse Compton scattering. CMB photons receive an average energy boost by collision with hot (a few keV) ionized electrons of the intra-cluster medium. The tSZ Compton parameter in a given direction, \mathbf{n} , on the sky is given by

$$y(\mathbf{n}) = \int n_e \frac{k_B T_e}{m_e c^2} \sigma_T ds \quad (1)$$

where ds is the distance along the line-of-sight, and n_e and T_e are the electron number-density and temperature. In units of CMB temperature, the tSZ effect at a frequency ν is

$$\frac{\Delta T_{\text{CMB}}}{T_{\text{CMB}}} = g(\nu) y. \quad (2)$$

Neglecting corrections due to the weakly relativistic high-end of the velocity distribution for the thermal electrons, we have

$$g(\nu) = \left[x \coth\left(\frac{x}{2}\right) - 4 \right], \quad (3)$$

with the dimensionless frequency $x = h\nu/(k_B T_{\text{CMB}})$. h and k_B represent the Planck and the Boltzmann constants. At $z = 0$, where $T_{\text{CMB}}(z = 0) = 2.726 \pm 0.001$ K, the tSZ effect signal is negative below 217 GHz and positive at higher frequencies. This characteristic spectral signature is a unique tool for detecting galaxy clusters. The spectral signature is directly related to T_{CMB} through the x variable. They depend on the convolution of the tSZ intensity with the *Planck* frequency responses.

4. Methodology

In this section, we describe the procedure that was used to extract the tSZ signal from the full-sky *Planck* intensity maps. We start by considering clusters from the *Planck* catalog, because they have a high signal-to-noise ratio and a low level of contamination. Then, we discuss the case of additional clusters from the samples listed in Sect. 2.3.

In a first step, we set all *Planck* frequency channels to a common angular resolution of $10'$, corresponding roughly to the angular resolution the lowest resolution channel at 100 GHz. Then, we extracted individual patches centered on the location of *Planck* galaxy clusters and stacked them. Next, we cleaned the obtained stacked patches from IR emission from galactic dust and extragalactic IR galaxies using the 857 GHz channel. Finally, we estimated the tSZ flux in each cleaned stacked patch.

4.1. Stacking

To increase the significance of the tSZ signal per frequency, we performed a stacking analysis in multiple redshift bins. Our sample consists of 813 clusters with known redshifts, distributed in 20 redshift bins from $z = 0$ to $z = 1$, with a binsize $\Delta z = 0.05$. The redshift bins and number of clusters per bin are listed in Table 3. Note that the mean redshift \bar{z} and the weighted mean over Y_{500} , z_{eff} only differs at the third decimal. This shows that the SZ flux distribution over the bin is homogeneous and that the choice of bins is a fair sampling of the redshift distribution for the considered cluster sample. In the following, we use z_{eff} as the mean value for our redshift bin.

We constructed a stacked patch per redshift bin. We thus extracted individual patches of $2^\circ \times 2^\circ$ from the full-sky intensity maps with pixels of $1.7'$. The individual patches were centered on the positions of the clusters in the considered redshift bin. The individual patches were re-projected using a nearest neighbor interpolation on a grid of $0.2'$ pixels in gnomonic projection. This conserves the cluster flux. Note that re-projection effects are the same for all frequencies and consequently do not bias the estimation of T_{CMB} since the latter only depends on the shape of the tSZ spectral law.

For each redshift bin individual patches are cleaned from point-source contamination. To do this, we masked all sources from the *Planck* Catalog of Compact Sources (Planck Collaboration 2014j) detected above 10σ in one of the six highest frequency channels of *Planck* within an area of $30'$ from the cluster center. Sources within a radius of $20'$ from the considered cluster were not masked. This process avoids biases in the dust-cleaning process (see Sect. 4.2).

Finally in each redshift bin, the individual patches per frequency were co-added with a constant weight. This choice is a two-fold one. It accounts for the fact that the main contribution to the noise due to CMB is similar from one patch to the other. Furthermore, it avoids cases where a particular cluster will dominate the stacked signal. It is worth noting that this a choice is not optimized for the signal-to-noise ratio of the flux.

We verified that we derive similar results when applying random rotations to the extracted patches before stacking. This test demonstrated that our stacking is not sensitive to specific orientations, produced, for example, by the thermal dust emission from the Galactic plane.

¹ We chose a constant patch size because the majority of clusters are point-like with respect to the adopted resolution of $10'$. Differences in the physical extension of clusters have thus no significant impact on our results.

4.2. Dust cleaning

To remove thermal dust contamination in stacked patches per frequency, we used the 857 GHz channel. The thermal dust emission is known to have a varying spectral energy distribution (SED) across the sky (Planck Collaboration 2013c). To compute the effective thermal dust SED for each stacked patch per frequency, we assumed that in a field of $2^\circ \times 2^\circ$ the thermal dust spectral properties can be well described by a single SED.

This cleaning was performed for each redshift bin δ and for each frequency i by computing the scale factor, ρ_i^δ , between the stacked patch at 857 GHz, M_{857}^δ , and other stacked patches from 100 to 545 GHz, M_i^δ . To avoid biases produced by correlations between IR emission and the tSZ effect, we computed ρ_i^δ by removing the central region of $r < 30'$, with r the angular distance to the clusters position. We checked that performing the cleaning per cluster instead of per redshift bin provides comparable results.

$$\rho_i^\delta = \frac{(\sum_{r>30'} M_{857}^\delta M_i) / n - (\sum_{r>30'} M_{857}^\delta) (\sum_{r>30'} M_i) / n^2}{(\sum_{r>30'} (M_{857}^\delta)^2) / n - (\sum_{r>30'} M_{857}^\delta)^2 / n^2}, \quad (4)$$

where n is the number of pixels satisfying the condition $r > 30'$. Then, the stacked patches cleaned from thermal dust were obtained by subtracting the 857 GHz from the other channels:

$$M_i^{\delta, \text{cleaned}} = M_i^\delta - \rho_i^\delta M_{857}^\delta. \quad (5)$$

This cleaning process has an impact solely on 353 and 545 GHz channels with ρ_i^δ values varying only by 10% and 5% at 353 and 545 GHz, from bin to bin. Dust-cleaned stacked patches for each redshift bin are presented in Figs. 1 and 2. We clearly observe (as reported in Planck Collaboration 2014i) the intensity decrement at low frequency (< 217 GHz), the null effect at 217 GHz and the positive emission at high frequency (> 217 GHz). Note that we report a clear detection of the tSZ effect even in the 545 GHz *Planck* channel for redshifts up to 0.6.

4.3. Flux estimate

To measure the flux from the cleaned stacked patches at 100, 143, 217, 353, and 545 GHz, we first derived the shape of the tSZ signal in the stacked patches. To do this, we computed a Compton- y parameter map for each cluster individually using the MILCA method (Hurier et al. 2013). Computing the y -map on a stacked patch would lead to a poorer tSZ reconstruction. We then stacked the reconstructed y -maps for the clusters within a given redshift bin. We refer to them as tSZ filter or template.

The tSZ signal in the stacked patches presents a circular symmetry. We therefore computed the radial profile of the tSZ filter and re-projected it to construct a denoised tSZ filter, M_{tSZ}^δ . We used M_{tSZ}^δ as a shape filter to measure the tSZ flux, F_i^δ , in each cleaned stacked patch $M_i^{\delta, \text{cleaned}}$.

The tSZ flux was obtained by computing a linear fit of the denoised tSZ filter on the cleaned stacked patches per frequency in a radius of $20'$ around the cluster center, assuming homogeneous noise and the following modeling

$$M_i^{\delta, \text{cleaned}} = F_i^\delta M_{\text{tSZ}}^\delta + b_i^\delta + N_i^\delta, \quad (6)$$

with b_i^δ a constant baseline accounting for large-scale ($> 20'$) residual contamination and N_i^δ the noise component including astrophysical emissions and instrumental noise.

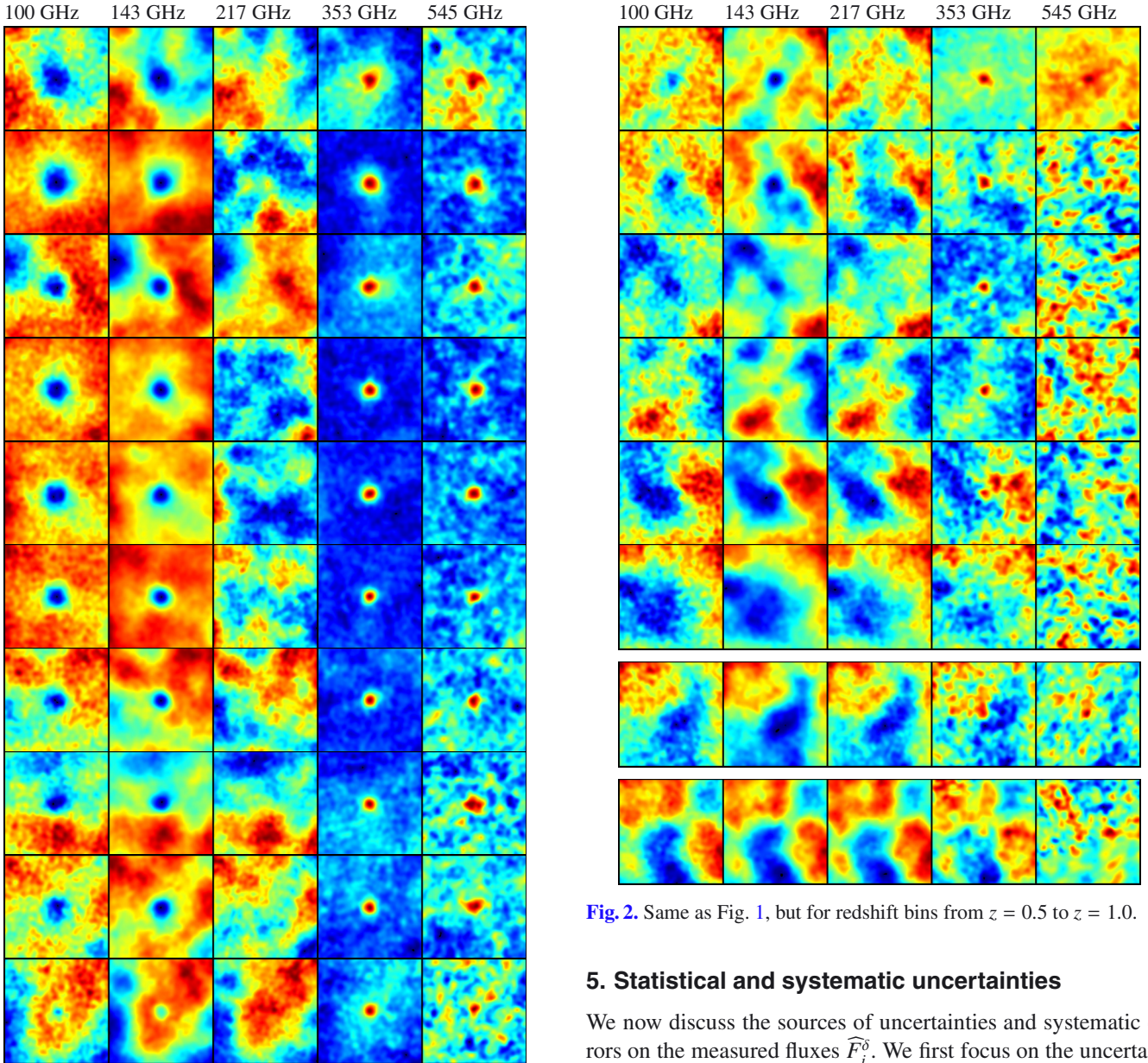


Fig. 1. From left to right: stack of *Planck* intensity maps from 100 to 545 GHz cleaned by the 857 GHz channel, centered on the location of *Planck* tSZ detected clusters. From top to bottom: stacked signal from tSZ detected clusters in different redshifts bins (from $z = 0.0$ to $z = 0.5$), see Table 4 for the redshift bins. Each stacked map represents an area of $2^\circ \times 2^\circ$.

From Eq. (6), we derived a tSZ emission law, \widehat{F}_i^δ , for each redshift bin δ . The estimator \widehat{F}_i^δ of F_i^δ was obtained by adjusting both F_i^δ and b_i^δ . Figure 3 presents the derived emission law for the tSZ effect for each redshift bin. The standard model is displayed as a dashed red line. Measured fluxes, \widehat{F}_i^δ , were used to derive the value of T_{CMB}^δ for each redshift bin in Sect. 6.

Note that using of a tSZ template induces no prior on the tSZ spectral law (considering that the spatial distribution of the tSZ signal is the same in all channels) and thus on \widehat{F}_i^δ . The small difference between tSZ filters from bin to bin is due to the difference in cluster extensions since the profiles used here were not rescaled with respect to their angular sizes contrary to Arnaud et al. (2010) and the Planck Collaboration (2013a).

Fig. 2. Same as Fig. 1, but for redshift bins from $z = 0.5$ to $z = 1.0$.

5. Statistical and systematic uncertainties

We now discuss the sources of uncertainties and systematic errors on the measured fluxes \widehat{F}_i^δ . We first focus on the uncertainties produced by background and foreground signals, including instrumental noise. Then we address the astrophysical components correlated to the tSZ emission, and finally we discuss the systematic errors caused by the instrument spectral responses.

5.1. Background and foreground contamination

To estimate the uncertainty on \widehat{F}_i^δ caused by contamination by other sources signal, we extracted the flux at 1000 random positions across the sky for each denoised tSZ filter. We avoided the galactic plane area, which is not represented in our cluster distribution.

In the stacking process each cluster was considered to be uncorrelated with others. Consequently, we derived the full covariance matrix for the flux estimate in frequency channels from 100 to 545 GHz. An example of correlation matrix is presented in Table 2. This correlation matrix only accounts for uncertainties produced by uncorrelated components (with respect to the tSZ effect) in the flux estimation. This correlation matrix has a determinant of 10^{-4} , which quantifies the volume occupied by the swarm of data samples in our five-dimension subspace (cleaned frequencies from 100 to 545 GHz).

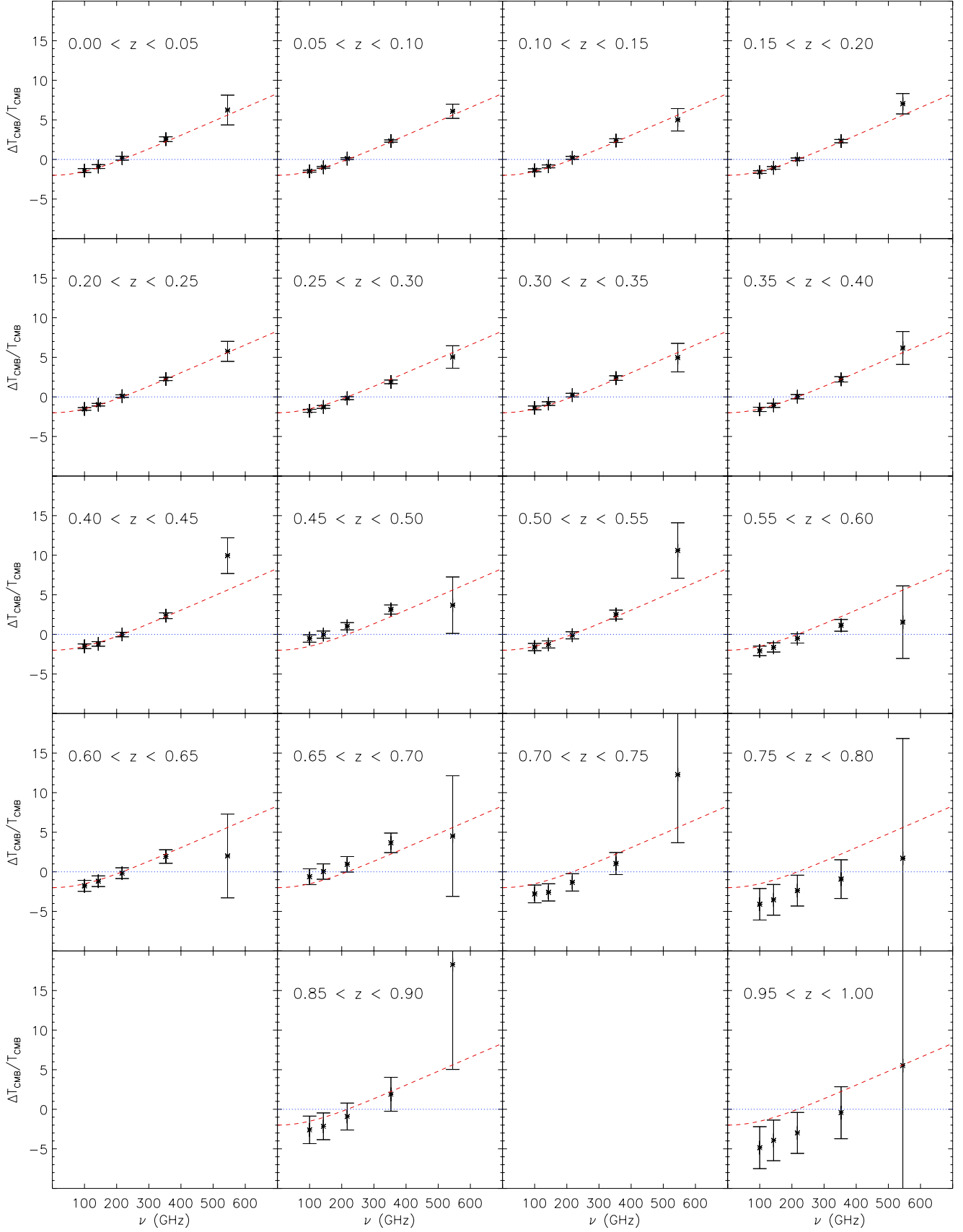


Fig. 3. From left to right and top to bottom: measured tSZ emission law in units of K_{CMB} for each redshift bin from 0 to 1, with $\Delta z = 0.05$. Note that bins with $0.80 \leq z < 0.85$ and $0.90 \leq z < 0.95$ do not contain any cluster. Black stars denote the data and dashed red lines the theoretical tSZ emission law. Error bars are strongly correlated between the different frequency channels, see Table 2.

Table 2. Correlation matrix of statistical uncertainties for the measurement of tSZ flux \widehat{F}_i^δ , estimated from 1000 random positions across the sky.

Frequency (GHz)	100	143	217	353	545
100	1	0.97	0.96	0.79	0.23
143	0.97	1	0.99	0.83	0.26
217	0.96	0.99	1	0.86	0.32
353	0.79	0.83	0.86	1	0.61
545	0.23	0.26	0.32	0.61	1

At 100 to 217 GHz, the CMB anisotropies are the main source of uncertainties. This explains the high level of correlation in the estimated fluxes. At higher frequencies, instrumental noise and dust residuals become an important contribution to the total uncertainties, which explains the lower level of correlation.

5.2. Correlated foreground contamination

Uncertainties produced by uncorrelated foregrounds, for instance, CMB, can be fairly estimated from measurements at random positions over the sky. However, these measurements do not account for noise or bias produced by correlated emissions, such as, radio sources at low frequency, cosmic infrared background (CIB) at high frequency, and the kinetic SZ effect.

5.2.1. Cosmic infrared background

The CMB temperature measure is directly related to the frequency at which tSZ effect is null, making it a key frequency in our analysis. At 217 GHz, a contribution from the CIB (the integrated IR emission from dust in distant galaxies (see e.g., Hauser & Dwek 2001; Kashlinsky 2005; Lagache et al. 2005, for reviews)) is significant and is correlated to the tSZ signal (e.g., Addison et al. 2012). In the following, we assumed a conservative situation of full correlation between tSZ and CIB, $\rho_{\text{cor}}^\delta = 1$. Note that the cluster sample used here does not contain all clusters at $z < 1$. Consequently, the actual correlation factor ρ_{cor}^δ is lower than one and depends on the completeness with respect to the redshift (see Planck Collaboration 2014i, for more details).

Considering the CIB intensity at 217 GHz, $\ell C_\ell^{\text{CIB}} = 0.25 \mu\text{K}^2 \cdot \text{sr}$, given by the Planck Collaboration (2011c), the CMB power spectrum at $\ell = 1000$, $\ell C_\ell^{\text{CMB}} \approx 1 \mu\text{K}^2 \cdot \text{sr}$, given in Planck Collaboration (2014f) and considering the contribution to tSZ power spectrum from our sample $\ell C_\ell^{\text{tSZ}} \approx 0.2 \times 10^{-15} \text{ y}^2 \text{ sr}$ (Planck Collaboration 2014h), we can compute the bias due to the CIB contribution. We furthermore assumed that 90% of the CIB is cleaned by the dust-cleaning process discussed in Sect. 4.2 and we defined $f_{\text{clean}} = 0.9$.

We used the following equation for the bias induced by tSZ \times CIB correlation for a given redshift bin δ :

$$B_{\text{CIB}}^\delta = \rho_{\text{cor}}^\delta \frac{f_{\text{CIB}}}{N_{\text{bin}}} \sqrt{\frac{C_\ell^{\text{CIB}}}{g(v_i)^2 C_\ell^{\text{tSZ}}}} \frac{F_i^\delta}{(\Delta F^\delta)_{\text{CMB}}} (1 - f_{\text{clean}}), \quad (7)$$

$f_{\text{CIB}} \sim 0.05$ is the fraction of CIB emission produced by objects at redshift < 1 , N_{bin} is the number of redshift bins, and $(\Delta F^\delta)_{\text{CMB}}$ is the contribution of the CMB to the uncertainties over F_i^δ .

We derived a ratio between CMB and CIB fluctuations of about 0.2% on average per cluster. At most, we use about one hundred clusters in a single redshift bin. This reduced the CMB fluctuations by a factor 10. Consequently, in a conservative case,

Table 3. Reshift binning used for our analysis.

Redshift bin δ	N_{cl}	\bar{z}	z_{eff}	F_{sync}^δ (%)
0.00–0.05	43	0.036	0.037	14.0
0.05–0.10	125	0.076	0.072	10.3
0.10–0.15	92	0.126	0.125	6.2
0.15–0.20	104	0.172	0.171	6.0
0.20–0.25	95	0.221	0.220	4.5
0.25–0.30	87	0.273	0.273	9.0
0.30–0.35	81	0.323	0.322	1.0
0.35–0.40	50	0.375	0.377	4.9
0.40–0.45	45	0.424	0.428	0.4
0.45–0.50	26	0.471	0.471	4.8
0.50–0.55	20	0.525	0.525	2.5
0.55–0.60	18	0.565	0.565	–0.5
0.60–0.65	12	0.619	0.618	2.5
0.65–0.70	6	0.676	0.676	–3.2
0.70–0.75	5	0.718	0.718	3.7
0.75–0.80	2	0.783	0.777	–2.8
0.80–0.85	0	–	–	–
0.85–0.90	1	0.870	0.870	–0.3
0.90–0.95	0	–	–	–
0.95–1.00	1	0.972	0.972	–0.3

Notes. N_{cl} is the number of clusters per bin, \bar{z} is the mean redshift, z_{eff} is the mean redshift weighted by the flux of each clusters Y_{500} (Planck Collaboration 2014i) and F_{sync}^δ is the radio contamination in tSZ measured flux at 100 GHz estimated from NVSS and SUMSS data. It is expressed in terms of percentage of the tSZ flux at 100 GHz.

the CIB at 217 GHz contributes at the level of 2% of the intensity of CMB and can therefore be neglected.

5.2.2. Radio point sources

Radio sources within galaxy clusters can produce an overestimate of the flux at low frequencies, which in turn leads to an underestimate of $T_{\text{CMB}}(z)$.

Using the NVSS and the SUMSS catalogs of radio point sources, we estimated the radio point-source contamination on the measured tSZ flux. To do this, we projected the NVSS and the SUMSS catalogs on a full-sky map (considering only SUMSS sources at Dec $< -40^\circ$, and extrapolating their fluxes from 853 MHz to 1.4 GHz with a spectral index of -1). Then, we smoothed the obtained map at $10'$. We thus obtained a full-sky map of the combined radio sources at 1.4 GHz on which we estimate the radio flux F_{rad}^δ for each stacked patch and redshift bin δ using the approach described in Sect. 4.3. Finally, we extrapolated the radio emission from 1.4 GHz to Planck frequencies, assuming a spectral index of -1 . We estimated the spectral index by computing the cross power spectrum between the NVSS catalog projected map and the Planck 100 GHz channel. We derived an averaged spectral index of -0.995 ± 0.010 .

The radio fluxes within the tSZ filter, F_{rad}^δ , expressed in terms of percentage of the measured tSZ flux at 100 GHz are summarized in Table 3. Under the simple assumption of a single spectral index -1 , we show that the contamination by radio source emission on the measured tSZ flux at 100 GHz is lower than 15%. In the analysis described in Sect. 6.2.2, we show how this contribution was modeled, fitted, and accounted for in the estimate of the uncertainties.

5.2.3. Kinetic Sunyaev-Zel'dovich effect

The kinetic SZ effect, kSZ, is the Doppler shift of CMB photons that scatter the intracluster electrons. This effect is faint, one order of magnitude lower than the tSZ. It has the same spectral dependence as the CMB and is spatially correlated to the tSZ signal. The kSZ effect can produce positive or negative CMB temperature anisotropies. Consequently, this effect will not bias the tSZ measurement, but will enlarge the CMB dispersion at the clusters position and therefore the error-bars. At *Planck* resolution, the increase in CMB variance due to the kSZ is small (Planck Collaboration 2013b) and can be neglected in our analysis.

In some nonstandard inhomogeneous cosmological models (see e.g. Goodman 1995; Clarkson 2012), the kSZ monopole is different from zero. This could induce a bias in the tSZ measurement. However, these models are now strongly constrained by *Planck* data (Planck Collaboration 2013b).

5.3. Effects of bandpass and calibration uncertainties

To measure the tSZ emission law in the *Planck* channels we integrated the tSZ emission law, $g(T_{\text{CMB}}^\delta, T_e^\delta, \nu)$ (see Eq. (3)), over the *Planck* spectral responses (i.e., bandpasses), see Planck Collaboration (2014b), H_i , in the following manner:

$$A_i(T_{\text{CMB}}^\delta, T_e^\delta) = \frac{\int H_i(\nu)g(T_{\text{CMB}}^\delta, T_e^\delta, \nu)d\nu}{\int H_i(\nu)C(\nu)d\nu}, \quad (8)$$

with, A_i the tSZ transmission in the i th *Planck* channel, $C(\nu)$ the emission law of the calibrators, CMB, and planets (Planck Collaboration 2014e), and T_e^δ the effective cluster temperature per redshift bin.

The bandpasses present uncertainties that depend on the tSZ spectral law. Given that T_{CMB}^δ and T_e^δ produce small variations of the tSZ, we can assume that the bandpass uncertainties are constant. We propagated the uncertainties on the bandpasses H_i in our analysis by computing the uncertainties on the tSZ emission law $A_i(T_{\text{CMB}}^\delta, T_e^\delta)$ after integrating over the bandpass. These turn into uncertainties on the recovered value of T_{CMB}^δ . We derived a systematic uncertainty of 0.010 K at $z = 0$ for T_{CMB}^δ ; it becomes $0.010 \times (1 + z_{\text{eff}})$ K for each redshift bin.

At low frequencies, the *Planck* data were calibrated with respect to CMB dipole ($T_{\text{CMB}}(z = 0)$). Uncertainties on the calibration can also lead to bias in $T_{\text{CMB}}^\delta(z)$. However, this source of uncertainties is small, about 0.2% at 100 to 217 GHz channels (Planck Collaboration 2014e). It was neglected in the following.

6. Analysis

6.1. Modeling the signal

Our measurement at the i th *Planck* frequency can be modeled as

$$F_i^\delta = Y^\delta A_i(T_{\text{CMB}}^\delta, T_e^\delta) + F_{\text{rad}}^\delta A_i^{\text{rad}} + F_{\text{ir}}^\delta A_i^{\text{ir}}, \quad (9)$$

with $Y^\delta = \int \int y d\Omega dz$ the integrated Compton parameter for a redshift bin δ , A_i^{rad} the radio source spectrum with spectral index -1 normalized to 1 at 100 GHz, and A_i^{ir} is the IR spectrum with dust temperature $T_d = 17$ K and spectral index $\beta_d = 1.8$ (Planck Collaboration 2011b) normalized to 1 at 353 GHz. We verified that this A_i^{ir} SED theoretical model is consistent with the spectrum derived from our cleaning procedure.

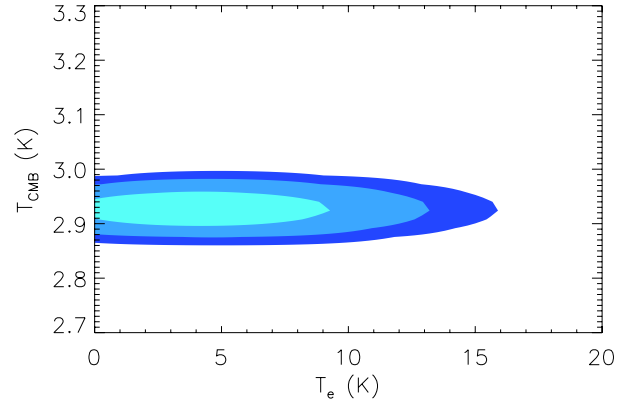


Fig. 4. Likelihood function of the measured tSZ emission law as a function of T_{CMB}^δ and T_e^δ for redshift bins between $z = 0.05$ and $z = 0.10$. Confidence levels at 1, 2, and 3σ are presented in light-blue, blue, and dark-blue areas.

The adjustable parameters are Y^δ , T_{CMB}^δ , T_e^δ , F_{rad}^δ the radio source flux and F_{ir}^δ the IR contamination level including CIB emission.

6.2. Sensitivity analysis

In the following, we perform a sensitivity analysis between T_{CMB}^δ and the other parameters of the model.

6.2.1. Impact of relativistic corrections

The relativistic corrections to the tSZ emission law has been computed numerically (see e.g. Rephaeli 1995; Pointecouteau et al. 1998; Itoh et al. 1998). If we assume that the relativistic corrections can be described as a first-order approximation,

$$\Delta T_{\text{CMB}}^{\text{relat}}(T_e) = \Delta T_{\text{CMB}}^{\text{unrelat}} + T_e^\delta \Delta T_{\text{CMB}}^{\text{cor}}, \quad (10)$$

the averaged tSZ emission law can be described with an averaged temperature fitted as an effective temperature, T_e^δ , for the stacked tSZ signal (see Nozawa et al. 2000, for a more detailed fitting formula).

Figure 4 presents the likelihood function in the plane (T_{CMB}^δ , T_e^δ) for clusters in the redshift bin 0.05 to 0.10. The other redshift bins present similar behaviors. The value we derived for T_e^δ is below 10 keV at 1σ level and below 15 keV at 3σ level, with a best-fitting value around 5 keV. This is consistent with the X-ray derived temperatures for typical clusters in the *Planck* sample. Figure 4 shows no correlation between the recovered value of T_{CMB}^δ and T_e^δ . This indicates that we can safely neglect relativistic corrections in our analysis.

6.2.2. Radio and IR contaminations

Figure 5 presents the likelihood function in the plane of the radio contamination, F_{rad}^δ , and T_{CMB}^δ (top panel), and in the plane of the IR contamination, F_{ir}^δ , and T_{CMB}^δ (bottom panel) for clusters within a redshift bin 0.10 to 0.15. The other redshift bins present similar behaviors. We found that the IR contamination, including CIB residuals, is compatible with 0 and does not bias our estimate of the tSZ flux. We also note that the derived value of F_{ir}^δ is consistent with all $f_{\text{clean}} > 0.8$ at 6σ level, consistent with the conservative case discussed in Sect. 5.2.1.

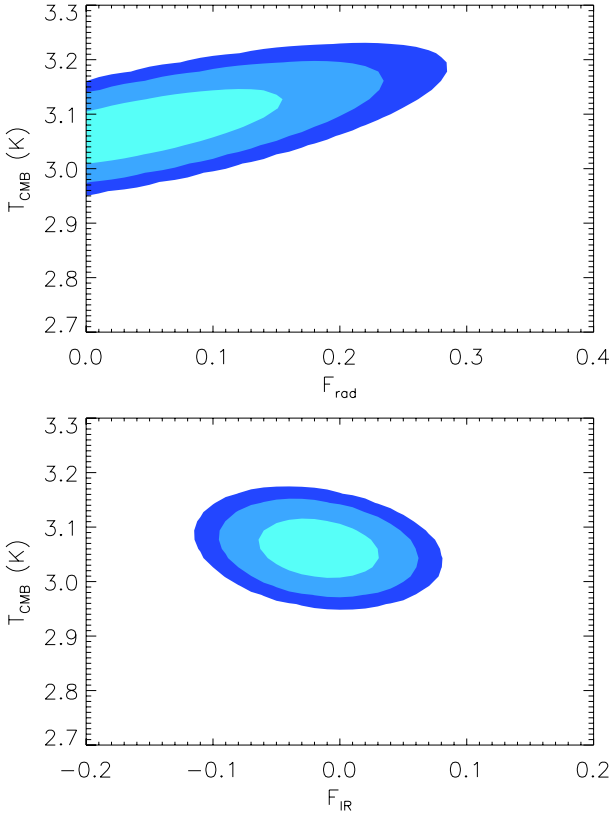


Fig. 5. *Top panel:* Likelihood function of the measured tSZ emission law as a function of T_{CMB}^δ and the radio source flux, expressed in units of tSZ flux at 100 GHz, for redshifts between $z = 0.10$ and $z = 0.15$. *Bottom panel:* Likelihood function of the measured tSZ emission law as a function of T_{CMB}^δ and the infrared contamination level, expressed in units of tSZ flux at 353 GHz, for redshift between $z = 0.10$ and $z = 0.15$. Confidence levels at 1, 2, and 3σ are represented in light-blue, blue, and dark-blue.

Furthermore, we observed that the radio source contamination produces some bias on the T_{CMB}^δ measurement. This bias translates into $\widehat{T}_{\text{CMB}}^\delta = T_{\text{CMB}}^\delta - 0.005 \times (1 + z_{\text{eff}}) \times F_{\text{rad}}^\delta$.

6.3. Profile likelihood analysis

Given the results of the sensitivity analysis discussed above, we can simplify the model in Eq. (9) to

$$F_i^\delta = Y^\delta A_i(T_{\text{CMB}}^\delta) + F_{\text{rad}}^\delta A_i^{\text{rad}}, \quad (11)$$

considering only the relevant parameters Y^δ , T_{CMB}^δ and F_{rad}^δ .

To fit T_{CMB}^δ in each redshift bin, we used a profile likelihood approach. First, we computed, through an unbiased linear fit, the tSZ flux, \widehat{Y}^δ , of our measured spectral law for each value of T_{CMB}^δ and F_{rad}^δ . Given the similar amplitudes of the uncertainties on the measurement (mainly CMB contamination) and the model (bandpasses), we used the following estimator for Y^δ :

$$\widehat{Y}^\delta = [A^T \mathcal{W} A - \text{Tr}(C_A^T \mathcal{W})]^{-1} [A^T \mathcal{W} \widehat{\mathbf{F}}^\delta], \quad (12)$$

with \mathbf{A} the tSZ transmission vector defined in Eq. (8), C_A the \mathbf{A} covariance matrix², $\widehat{\mathbf{F}}^\delta$ the measured tSZ emission law (see

² The uncertainties on the response A_i^{rad} are lower than 1% and neglected. In contrast, the uncertainties on the response for the tSZ in the 217 GHz channel is about 25% (Planck Collaboration 2014b).

Table 4. Measured value of T_{CMB}^δ in Kelvin derived from the tSZ emission law per redshift bin.

Redshift bin δ	N_{cl}	T_{CMB}^δ	ΔT_{CMB} (stat)	ΔT_{CMB} (syst)
0.00–0.05	43	2.888	0.039	0.011
0.05–0.10	125	2.931	0.017	0.011
0.10–0.15	92	3.059	0.032	0.012
0.15–0.20	104	3.197	0.030	0.012
0.20–0.25	95	3.288	0.032	0.013
0.25–0.30	87	3.416	0.038	0.013
0.30–0.35	81	3.562	0.050	0.014
0.35–0.40	50	3.717	0.063	0.014
0.40–0.45	45	3.971	0.071	0.015
0.45–0.50	26	3.943	0.112	0.015
0.50–0.55	20	4.380	0.119	0.016
0.55–0.60	18	4.075	0.156	0.016
0.60–0.65	12	4.404	0.194	0.016
0.65–0.70	6	4.779	0.278	0.017
0.70–0.75	5	4.933	0.371	0.017
0.75–0.80	2	4.515	0.621	0.018
0.80–0.85	0	–	–	–
0.85–0.90	1	5.356	0.617	0.019
0.90–0.95	0	–	–	–
0.95–1.00	1	5.813	1.025	0.020

Notes. Systematic errors are fully correlated from one redshift bin to the next.

Eq. (6)), and $\mathcal{W} = C_{F^\delta}^{-1}$ the inverse of the noise covariance matrix on $\widehat{\mathbf{F}}^\delta$.

Then, we computed the χ^2 , for each paire of parameters (T_{CMB}^δ , F_{sync}^δ) as

$$\chi^2 = (\widehat{\mathbf{F}}^\delta - \mathbf{F}^\delta)^T [C_{F^\delta} + (\widehat{Y}^\delta)^2 C_A]^{-1} (\widehat{\mathbf{F}}^\delta - \mathbf{F}^\delta). \quad (13)$$

Finally, we estimated the value of T_{CMB}^δ by marginalizing over F_{rad}^δ , considering a flat prior $-5\% < F_{\text{rad}}^\delta < 15\%$ (as observed in Sect. 5.2.2); and by computing the first-order moment of the likelihood function, $\mathcal{L} = e^{-\chi^2/2}$ with respect to T_{CMB}^δ ³.

We computed the uncertainties on T_{CMB}^δ using the second-order moment of \mathcal{L} . Note that the uncertainties only differ at the fourth decimal at 68% confidence level. We also computed the covariance between each T_{CMB}^δ and separated the statistical uncertainties that are fully uncorrelated between redshift bins, and the systematic errors that are fully correlated from one bin to another.

Table 4 summarizes our results for the derived $T_{\text{CMB}}(z)$ and the associated statistical and systematic uncertainties. We verified that removing clusters contaminated by very bright radio sources ($S \geq 250$ mJy at 1.4 GHz) does not affect our results.

7. Results

The measurement of the tSZ emission law allows us to constrain the value of T_{CMB} at $z = 0$ and its redshift dependence. We explore these two constraints separately. We present the results for the sample of *Planck* clusters, which constitutes our base dataset. We also discuss other cluster samples and finally we give the tightest constraints obtained by combining tSZ measures from *Planck* clusters and measures from molecular and atomic absorptions.

³ Note that the obtained T_{CMB} value only differs at the third decimal when the maximum likelihood is used as estimator.

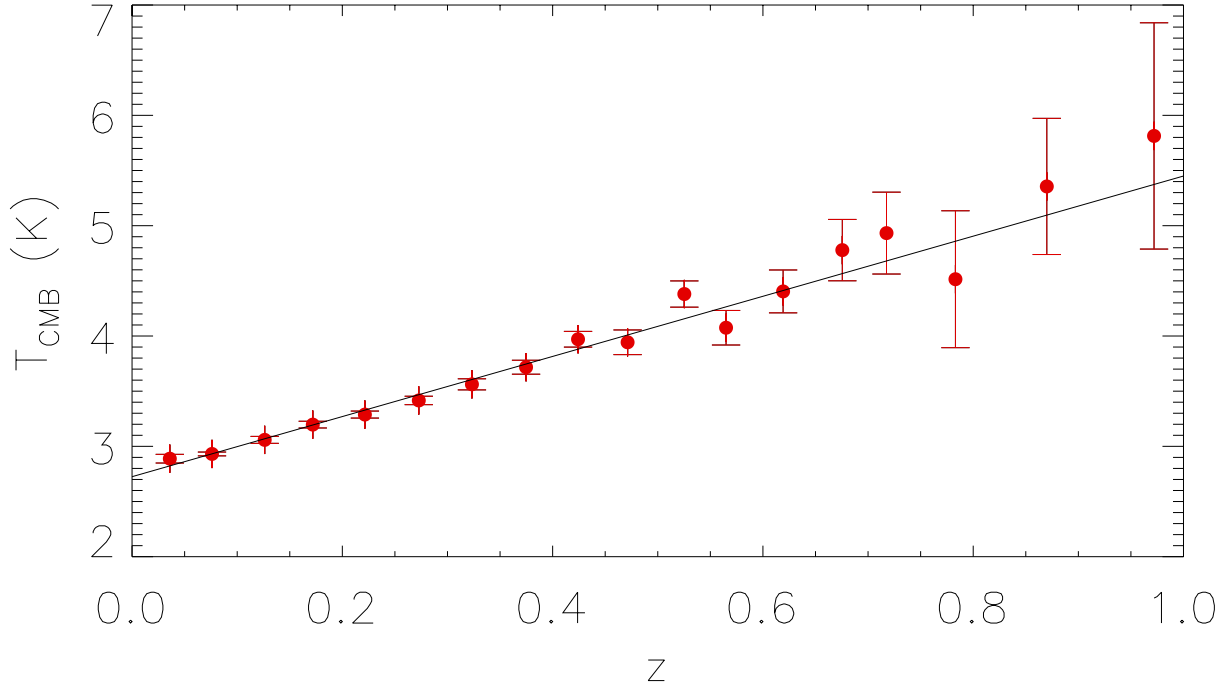


Fig. 6. Measured T_{CMB}^{δ} from the *Planck* data are shown as red filled circles. The theoretical $T_{\text{CMB}}(z)$ dependence in adiabatic expansion with $T_{\text{CMB}}(z = 0) = 2.726$ K is presented as black solid line. Note that the line is not a fit to the data points. Here, error bars only account for the statistical dispersion. The uncertainties due to spectral responses are not displayed.

7.1. Constraints on CMB temperature

We computed the χ^2 per degree of freedom (dof) between our measurements of T_{CMB}^{δ} (red filled circles in Fig. 6) and the adiabatic evolution of the CMB temperature (solid line in Fig. 6), with $T_{\text{CMB}}(z = 0) = 2.726 \pm 0.001$ K. We obtained $\chi_{\text{d.o.f.}}^2 = 0.89$. This implies that our measurements are consistent with the standard T_{CMB} evolution.

If we assume an adiabatic expansion, $T_{\text{CMB}}(z)$ is written as

$$T_{\text{CMB}}(z) = T_{\text{CMB}}(z = 0)(1 + z). \quad (14)$$

We derived $T_{\text{CMB}}(z = 0)$ from the estimated T_{CMB}^{δ} for all the redshift bins δ probed by our sample of *Planck* clusters. The measurements are presented in Fig. 6 as red filled circles. We observe that all measurements are within a 2σ from the adiabatic expansion evolution. The best fit, using all redshift bins, gives $T_{\text{CMB}}(z = 0) = 2.720 \pm 0.009 \pm 0.011$ K with statistical and systematics uncertainties, respectively. Note that the errors are dominated by the systematic uncertainty from the spectral responses. It is fully correlated between redshift bins, and thus cannot be reduced. Our measurement of $T_{\text{CMB}}(z = 0)$ from the tSZ emission law cannot compete, in terms of accuracy, with the COBE-FIRAS $T_{\text{CMB}}(z = 0) = 2.726 \pm 0.001$ K (Fixsen 2009). However, it is fully consistent.

7.2. Constraints on the redshift evolution

Our analysis was based on a sample of 813 *Planck* clusters covering a redshift range from 0 to 1. If we express $T_{\text{CMB}}(z)$ as in Lima et al. (2000),

$$T_{\text{CMB}}(z) = T_{\text{CMB}}(z = 0)(1 + z)^{1-\beta}, \quad (15)$$

it is possible to test the T_{CMB} evolution in adiabatic expansion. We fit β using a maximum-likelihood analysis and a flat prior. Figure 7 presents the best-fitting value of β for each individual

redshift bin δ , considering $T_{\text{CMB}}(z = 0) = 2.726$. We observe that all redshift bins are consistent with $\beta = 0$ at 2σ and that redshift bins from $z = 0.05$ to $z = 0.7$ provide similar constraints on β . Figure 7 also illustrates that our constraint on β are not dominated by a given bin, but that it uses the entire redshift range.

We derived $\beta = 0.009 \pm 0.017$ from the tSZ emission law in the 18 redshift bins used in the analysis, consistent with no deviation from adiabatic evolution. Note that in contrast to the $T_{\text{CMB}}(z = 0)$ measurement, β is not affected by bandpass uncertainties because they are fully correlated for all redshift bins.

We compared our result on β with the different constraints obtained either from other tSZ measurements or molecular and atomic absorptions.

Previous analyses have measured $T_{\text{CMB}}(z)$ either at low redshift (Luzzi et al. 2009) using the tSZ effect on a small number of clusters, or at higher redshifts (Cui et al. 2005; Ge et al. 1997; Sriand et al. 2000; Molaro et al. 2002; Muller et al. 2013) using atomic and molecular absorption. These T_{CMB} measurements are presented in Fig. 8 with the standard adiabatic evolution shown as a solid black line.

We derived for the above-mentioned measurements constraints on β using the same fitting procedure and a flat prior as in our analysis. Table 5 summarizes the results. We found that the tSZ emission law from *Planck* clusters provides the tightest constraint on β . Errors are smaller by about a factor of two compared with previous constraints, separately. Our result, $\beta = 0.009 \pm 0.017$, from tSZ effect in *Planck* clusters is at the same level of precision and accuracy as the tightest constraint, $\beta = 0.009 \pm 0.019$, reported by Muller et al. (2013), combining all the constraints from molecular and atomic lines and tSZ clusters before *Planck*.

By furthermore combining our new limit on β with the previous data sets, we improved the derived constraint on the T_{CMB} evolution. We found $\beta = 0.006 \pm 0.013$. It is worth noting that

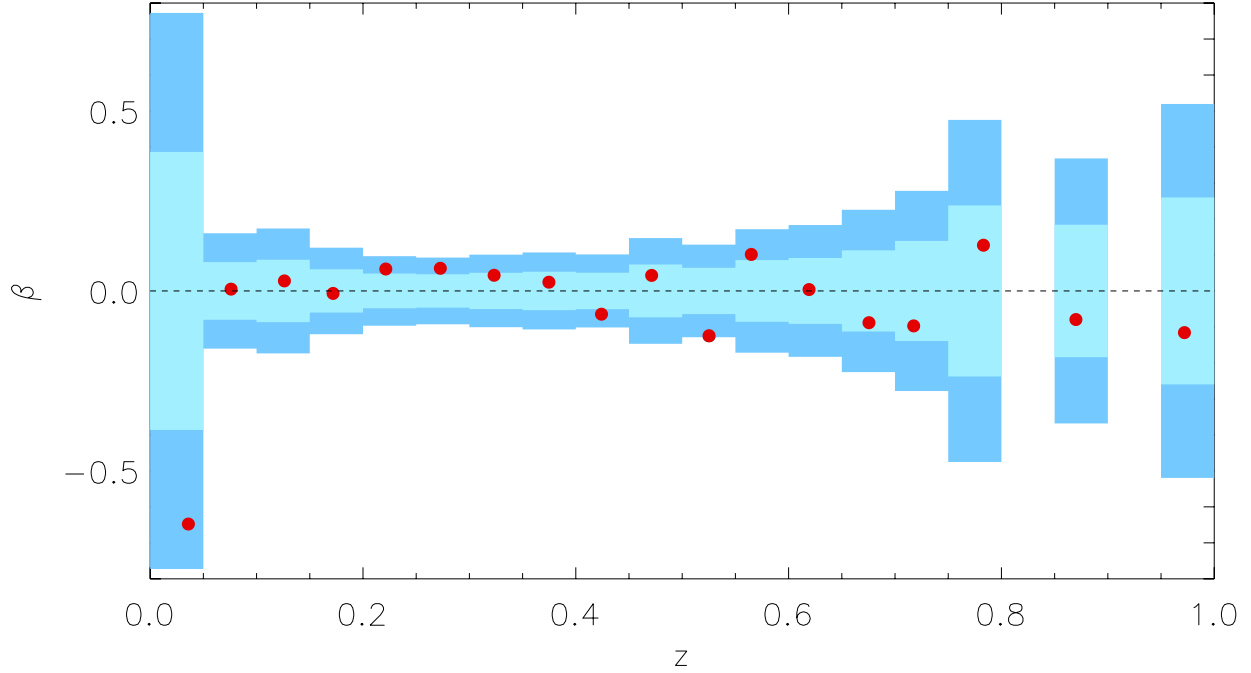


Fig. 7. Derived β values for each redshift bin δ considering $T_{\text{CMB}}(z=0) = 2.726$. Red filled circles show our measurements, light- and dark-blue shaded regions show the 1 and 2σ levels. Errors bars are displayed centered on $\beta = 0$ to facilitate the comparison between uncertainties in the different redshift bins δ . The dashed black line represents $\beta = 0$ for standard evolution.

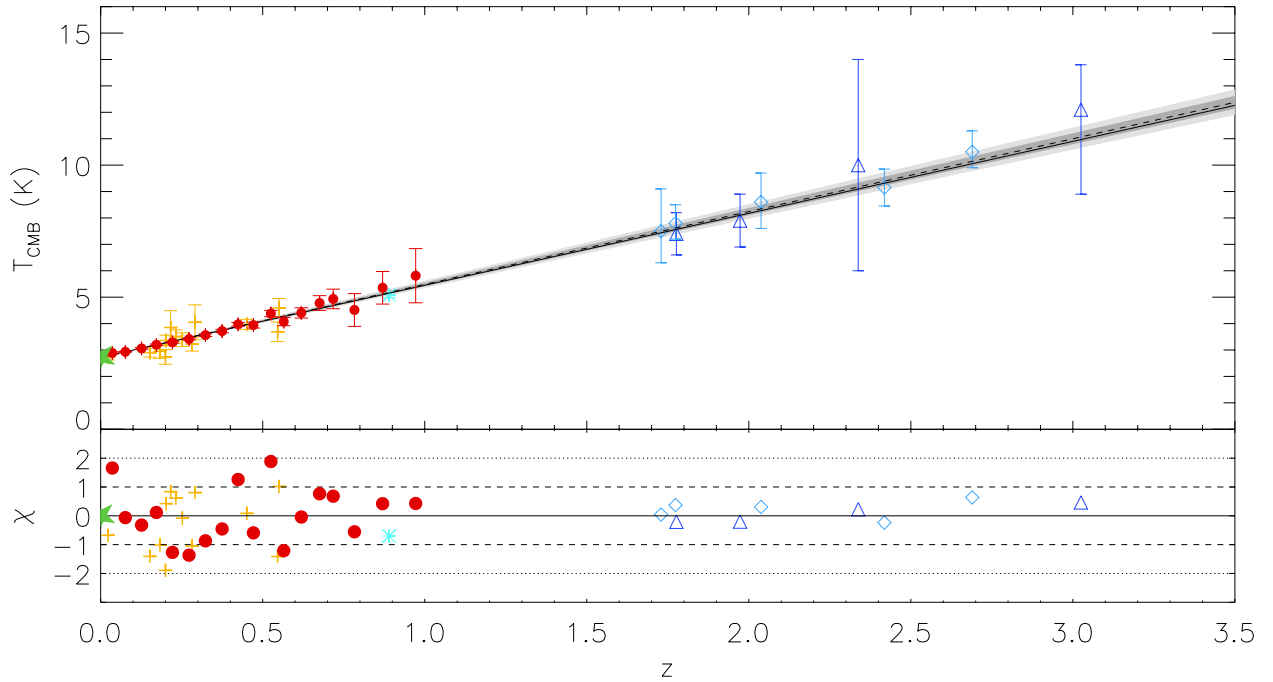


Fig. 8. *Top panel:* T_{CMB} as a function of redshift. The red filled circles represent T_{CMB} measured from the tSZ emission law in redshift bins of *Planck* clusters. The green star shows COBE-FIRAS measurement at $z = 0$ (Fixsen 2009). The orange crosses show T_{CMB} measurements using individual clusters (Battistelli et al. 2002; Luzzi et al. 2009). Dark-blue triangles represent measurements from C_{I} and C_{II} absorption (Cui et al. 2005; Ge et al. 1997; Srianand et al. 2000; Molaro et al. 2002) at $z = (1.8, 2.0, 2.3, 3.0)$. Blue diamonds show the measurements from CO absorption lines (Srianand et al. 2008; Noterdaeme et al. 2011), and finally the light-blue asterisk is the constraint from various molecular species analyses by Muller et al. (2013). The solid black line presents the standard evolution for T_{CMB} and the dashed black line represents our best-fitting model combining all the measurements. The 1 and 2σ envelopes are displayed as shaded dark and light-gray regions. *Bottom panel:* deviation from the standard evolution in units of standard deviation. The dashed and dotted black lines correspond to the 1 and 2σ levels.

in this combination the fit is driven by our own analysis and the measurements from Muller et al. (2013) and Noterdaeme et al. (2011) which have uncertainties of 0.017, 0.031, and 0.033, respectively.

8. Discussion

Our basic results presented in Sect. 7 were derived from the analysis of tSZ emission law of 813 clusters from *Planck* up to $z \sim 1$.

Table 5. Measured values of T_{CMB} and β re-derived, with our fitting procedure, from different subsamples of $T_{\text{CMB}}(z)$ measurements based on the tSZ effect and atomic/molecular absorptions.

Measurement method	T_{CMB}	ΔT_{CMB}	β	$\Delta\beta$	$\chi^2_{\text{d.o.f}}$	d.o.f.	References
C_I and C_{II} absorption	2.71	0.20	-0.002	0.067	0.09	4	(a)
CO absorption	2.78	0.11	-0.018	0.033	0.14	5	(b)
Various molecular species	2.69	0.05	0.022	0.031	0.52	1	(c)
tSZ	2.66	0.05	0.034	0.078	1.01	13	(d)
tSZ (this work)	2.72	0.01	0.009	0.017	0.89	18	(e)
All atomic and molecular	2.71	0.05	0.003	0.021	0.16	10	(a,b,c)
All tSZ	2.72	0.01	0.009	0.016	0.91	31	(d,e)
All	2.72	0.01	0.006	0.013	0.74	41	(a,b,c,d,e)

Notes. We provide the $\chi^2_{\text{d.o.f}}$ with respect to the standard adiabatic evolution with $T_{\text{CMB}} = 2.726 \pm 0.001$ K and $\beta = 0$. (a) using data samples from Cui et al. (2005); Ge et al. (1997); Srianand et al. (2000) and Molaro et al. (2002); (b) using data samples from Srianand et al. (2008) and Noterdaeme et al. (2011); (c) using data samples from Muller et al. (2013); (d) using data samples from Battistelli et al. (2002) and Luzzi et al. (2009); (e) the present analysis.

We found $\beta = 0.009 \pm 0.017$, which shows that even with a moderately deep sample tSZ is a competitive observational way of constraining the evolution of T_{CMB} .

To explore the variation of this result with other cluster samples, we performed the same analysis, as in Sect. 6, on the MCXC (Piffaretti et al. 2011) catalog. This allowed us to select a large number of massive clusters (see Table 1). To avoid significant radio contamination of the tSZ measurement, we considered only clusters with an intensity lower than $500 \mu\text{K}_{\text{CMB}}$ in the 100 GHz channel. This process only removes three clusters from our initial MCXC sample (see Sect. 2.3). We thus performed our analysis, and with the obtained T_{CMB} measures ranging from $z = 0$ to 0.35, we found $\beta = 0.07 \pm 0.10$. This poor constraint is mainly due to the reduced redshift range and to the relatively low tSZ flux associated with a large portion of the considered clusters. We also analyzed the SPT (Reichardt et al. 2013) and ACT (Hasselfield et al. 2013) catalogs. Again, we derived poor constraints on β , because the tSZ signal in the *Planck* intensity maps from the selected clusters is faint. Consequently, we did not include these measurements in the analysis. Combining the constraints from the tSZ emission law with other direct measurement using molecular and atomic absorption, we found the tightest limit on the T_{CMB} evolution to be $\beta = 0.006 \pm 0.013$, consistent with a standard T_{CMB} evolution.

Departures from an adiabatic evolution of T_{CMB} can be tested through indirect measurements. In particular when CMB photon number is not conserved, β can be constrained by the distance duality relation violation (Aygoustidis et al. 2012, and references therein) or by combining the CMB and galaxy distribution (as in, e.g., Opher & Pelinson 2005). These indirect measurements yield $\beta = 0.010 \pm 0.020$ and $\beta \leq 0.0034$, consistent with our analysis. Our tSZ-based measurements can also test deviations from the T_{CMB} -redshift relation in decaying dark-energy (DE) models. Jetzer et al. (2011) predicted the following relation:

$$T_{\text{CMB}}(z) = T_{\text{CMB}}(z=0) \times (1+z) \times \left(\frac{(m-3)\Omega_m + m(1+z)^{m-3}\Omega_\Lambda}{(m-3)\Omega_m} \right)^{1/3}, \quad (16)$$

with Ω_m and Ω_Λ the matter and DE energy densities at $z = 0$, and $m = 3(w_{\text{eff}} + 1)$ is related to the effective equation of state of the decaying DE, w_{eff} . Considering a flat Universe and $\Omega_m = 0.314 \pm 0.020$ (Planck Collaboration 2014g), we derive $w_{\text{eff}} = -0.995 \pm 0.011$, which improves previous constraint from Noterdaeme et al. (e.g., 2011).

The evolution of T_{CMB} with redshift can also be affected by time-varying fundamental constants (see Uzan 2011, for a recent review). Specifically for the tSZ-based constraints, variations of h and k_B in Eq. (3) lead to deviations of β from zero $\frac{h}{k_B T_{\text{CMB}}(0)}(1+z)^\beta = C^{\text{ste}}$. However, variations of the fundamental constants become small after the Universe enters its current DE-dominated epoch (Barrow et al. 2002), and consequently tSZ variations are less sensitive to these changes at $z < 1$.

9. Conclusion

We have performed an analysis of the *Planck* intensity data in the range of 100 to 857 GHz, aimed at deriving the CMB temperature and its evolution via the tSZ emission law. Based on the *Planck* SZ catalog, we measured $T_{\text{CMB}}(z)$ in the redshift range $0 < z < 1$. This is the first measurement of $T_{\text{CMB}}(z)$ on such a large tSZ sample of clusters. It demonstrates the ability of exploring the low-redshift range which cannot be covered by the traditionally used optical/UV quasar absorption systems.

We showed that clustered CIB and relativistic corrections to the tSZ spectral law do not produce any significant bias on our result. We note that the main uncertainties are caused by the *Planck* instrumental spectral responses, CMB contamination, and the radio source contamination. They were modeled and accounted for in the error bars in the determination of $T_{\text{CMB}}(z)$.

Our measurement of $T_{\text{CMB}}(z)$ below $z = 1$ reaches a precision of about 5% below $z = 0.65$, about 1% for all bins below $z = 0.3$, and better than 0.6% for the redshift between $z = 0.05$ and $z = 0.10$. This is the most precise measurement at $z > 0$ to date. Combining $T_{\text{CMB}}(z)$ at low redshifts with results from Muller et al. (2013) and references presented in Fig. 8, we obtained the tightest constraints so far on the $T_{\text{CMB}}(z) = T_{\text{CMB}}(z=0)(1+z)^{1-\beta}$ law, with $\beta = 0.006 \pm 0.013$. Our result confirms that the CMB temperature evolution is consistent with an adiabatic expansion.

The discovery of new massive high- z ($z > 0.5$) clusters will bring a major improvement in $T_{\text{CMB}}(z)$ measurement from the tSZ emission law. In particular, SZ surveys such as *Planck* and SPT-3G and optical surveys such as the Dark Energy Survey (The Dark Energy Survey Collaboration 2005) and Pan-STARRS (Kaiser et al. 2002; Tonry et al. 2012) will provide us with much larger and deeper cluster samples. In the future, even larger and deeper samples of massive clusters will be constructed from from EUCLID (Amiaux et al. 2012; Amendola et al. 2013), the Large Synoptic Survey Telescope (LSST Science Collaboration et al. 2009), and SRG-eROSITA

(Merloni et al. 2012; Pillepich et al. 2012). In combination with the fourth-generation CMB space mission, the tSZ emission law from clusters will strongly improve existing constraints on $T_{\text{CMB}}(z)$ up to $z = 2$.

Acknowledgements. We thank the anonymous referee for his or her comments. We are grateful to J. F. Macías-Pérez, J. M. Diego, and R. Genova-Santos for their comments and suggestions. Some of the results in this paper have been derived using the HEALPix package (Górski et al. 2005). We acknowledge the support of the French *Agence Nationale de la Recherche* under grant ANR-11-BD56-015. The development of Planck has been supported by: ESA; CNES and CNRS/INSU-IN2P3-INP (France); ASI, CNR, and INAF (Italy); NASA and DoE (USA); STFC and UKSA (UK); CSIC, MICINN and JA (Spain); Tekes, AoF and CSC (Finland); DLR and MPG (Germany); CSA (Canada); DTU Space (Denmark); SER/SSO (Switzerland); RCN (Norway); SFI (Ireland); FCT/MCTES (Portugal); and The development of Planck has been supported by: ESA; CNES and CNRS/INSU-IN2P3-INP (France); ASI, CNR, and INAF (Italy); NASA and DoE (USA); STFC and UKSA (UK); CSIC, MICINN and JA (Spain); Tekes, AoF and CSC (Finland); DLR and MPG (Germany); CSA (Canada); DTU Space (Denmark); SER/SSO (Switzerland); RCN (Norway); SFI (Ireland); FCT/MCTES (Portugal); and PRACE (EU).

References

- Addison, G. E., Dunkley, J., & Spergel, D. N. 2012, MNRAS, 427, 1741
 Amendola, L., Appleby, S., Bacon, D., et al. 2013, Liv. Rev. Rel., 16, 6
 Amiaux, J., Scaramella, R., Mellier, Y., et al. 2012, in SPIE Conf. Ser., 8442
 Arnaud, M., Pratt, G. W., Piffaretti, R., et al. 2010, A&A, 517, A92
 Avgoustidis, A., Luzzi, G., Martins, C. J. A. P., & Monteiro, A. M. R. V. L. 2012, JCAP, 2, 13
 Bahcall, J. N., & Wolf, R. A. 1968, ApJ, 152, 701
 Barrow, J. D., Sandvik, H. B., & Magueijo, J. 2002, Phys. Rev. D, 65, 063504
 Battistelli, E. S., De Petris, M., Lamagna, L., et al. 2002, ApJ, 580, L101
 Bennett, C. L., Halpern, M., Hinshaw, G., et al. 2003, ApJS, 148, 1
 Chang, C. L., Ade, P. A. R., Aird, K. A., et al. 2009, in AIP Conf. Ser., 1185, eds. B. Young, B. Cabrera, & A. Miller, 475
 Clarkson, C. 2012, C. R. Phys., 13, 682
 Combes, F., & Wiklind, T. 1999, in Highly Redshifted Radio Lines, eds. C. L. Carilli, S. J. E. Radford, K. M. Menten, & G. I. Langston, ASP Conf. Ser., 156, 210
 Condon, J. J., Cotton, W. D., Greisen, E. W., et al. 1998, AJ, 115, 1693
 Cui, J., Bechtold, J., Ge, J., & Meyer, D. M. 2005, ApJ, 633, 649
 de Martino, I., Atrio-Barandela, F., da Silva, A., et al. 2012, ApJ, 757, 144
 Fabbri, R., Melchiorri, F., & Natale, V. 1978, Ap&SS, 59, 223
 Fixsen, D. J. 2009, ApJ, 707, 916
 Fixsen, D. J., Cheng, E. S., Gales, J. M., et al. 1996, ApJ, 473, 576
 Freese, K., Adams, F. C., Frieman, J. A., & Mottola, E. 1987, Nucl. Phys. B, 287, 797
 Ge, J., Bechtold, J., & Black, J. H. 1997, ApJ, 474, 67
 Goodman, J. 1995, Phys. Rev. D, 52, 1821
 Górski, K. M., Hivon, E., Banday, A. J., et al. 2005, ApJ, 622, 759
 Hasselfield, M., Hilton, M., Marriage, T. A., et al. 2013, JCAP, 07, 008
 Hauser, M. G., & Dwek, E. 2001, ARA&A, 39, 249
 Hincks, A. D., Acquaviva, V., Ade, P. A. R., et al. 2010, ApJS, 191, 423
 Horellou, C., Nord, M., Johansson, D., & Lévy, A. 2005, A&A, 441, 435
 Hurier, G., Hildebrandt, S. R., & Macias-Perez, J. F. 2013 [arXiv:1007.1149]
 Itoh, N., Kohyama, Y., & Nozawa, S. 1998, ApJ, 502, 7
 Jaeckel, J., & Ringwald, A. 2010, Ann. Rev. Nucl. Sci., 60, 405
 Jetzer, P., Puy, D., Signore, M., & Tortora, C. 2011, Gen. Relativ. Gravit., 43, 1083
 Kaiser, N., Aussen, H., Burke, B. E., et al. 2002, in SPIE Conf. Ser. 4836, eds. J. A. Tyson, & S. Wolff, 154
 Kashlinsky, A. 2005, Phys. Rep., 409, 361
 Lagache, G., Puget, J.-L., & Dole, H. 2005, ARA&A, 43, 727
 Lima, J. A. S., & Trodden, M. 1996, Phys. Rev. D, 53, 4280
 Lima, J. A. S., Silva, A. I., & Viegas, S. M. 2000, MNRAS, 312, 747
 Losocco, J. M., Mathews, G. J., & Wang, Y. 2001, Phys. Rev. D, 64, 123002
 LSST Science Collaboration, Abell, P. A., Allison, J., et al. 2009 [arXiv:0912.0201]
 Lu, L., Sargent, W. L. W., Barlow, T. A., Churchill, C. W., & Vogt, S. S. 1996, ApJS, 107, 475
 Luzzi, G., Shimon, M., Lamagna, L., et al. 2009, ApJ, 705, 1122
 Mather, J. C., Fixsen, D. J., Shafer, R. A., Mosier, C., & Wilkinson, D. T. 1999, ApJ, 512, 511
 Matyjasek, J. 1995, Phys. Rev. D, 51, 4154
 Mauch, T., Murphy, T., Buttery, H. J., et al. 2003, MNRAS, 342, 1117
 Mauch, T., Murphy, T., Buttery, H. J., et al. 2008, VizieR Online Data Catalog: VIII/081
 Merloni, A., Predehl, P., Becker, W., et al. 2012 [arXiv:1209.3114]
 Meyer, D. M., York, D. G., Black, J. H., Chaffee, Jr., F. H., & Foltz, C. B. 1986, ApJ, 308, L37
 Molaro, P., Levshakov, S. A., Dessauges-Zavadsky, M., & D'Odorico, S. 2002, A&A, 381, L64
 Muller, S., Beelen, A., Black, J. H., et al. 2013, A&A, 551, A109
 Murphy, M. T., Webb, J. K., & Flambaum, V. V. 2003, MNRAS, 345, 609
 Noterdaeme, P., Petitjean, P., Srianand, R., Ledoux, C., & López, S. 2011, A&A, 526, L7
 Nozawa, S., Itoh, N., Kawana, Y., & Kohyama, Y. 2000, ApJ, 536, 31
 Opher, R., & Pelinson, A. 2005, Braz. J. Phys., 35, 1206
 Overduin, J. M., & Cooperstock, F. I. 1998, Phys. Rev. D, 58, 043506
 Piffaretti, R., Arnaud, M., Pratt, G. W., Pointecouteau, E., & Melin, J.-B. 2011, A&A, 534, A109
 Pillepich, A., Porciani, C., & Reiprich, T. H. 2012, MNRAS, 422, 44
 Planck Collaboration 2011a, A&A, 536, A8
 Planck Collaboration 2011b, A&A, 536, A19
 Planck Collaboration 2011c, A&A, 536, A18
 Planck Collaboration 2011d, A&A, 536, A26
 Planck Collaboration 2013a, A&A, 550, A131
 Planck Collaboration 2013b, A&A, 561, A97
 Planck Collaboration 2013c, A&A, submitted [arXiv:1307.6815]
 Planck Collaboration 2014a, A&A, submitted [arXiv:1303.5062]
 Planck Collaboration 2014b, A&A, submitted [arXiv:1303.5070]
 Planck Collaboration 2014c, A&A, submitted [arXiv:1303.5067]
 Planck Collaboration 2014d, A&A, submitted [arXiv:1303.5068]
 Planck Collaboration 2014e, A&A, submitted [arXiv:1303.5069]
 Planck Collaboration 2014f, A&A, submitted [arXiv:1303.5075]
 Planck Collaboration 2014g, A&A, submitted [arXiv:1303.5076]
 Planck Collaboration 2014h, A&A, submitted [arXiv:1303.5081]
 Planck Collaboration 2014i, A&A, submitted [arXiv:1303.5089]
 Planck Collaboration 2014j, A&A, submitted [arXiv:1303.5088]
 Pointecouteau, E., Giard, M., & Barret, D. 1998, A&A, 336, 44
 Puy, D. 2004, A&A, 422, 1
 Reichardt, C. L., Stalder, B., Bleem, L. E., et al. 2013, ApJ, 763, 127
 Rephaeli, Y. 1980, ApJ, 241, 858
 Rephaeli, Y. 1995, ARA&A, 33, 541
 Roth, K. C., & Bauer, J. M. 1999, ApJ, 515, L57
 Roth, K. C., Meyer, D. M., & Hawkins, I. 1993, ApJ, 413, L67
 Song, J., Zenteno, A., Stalder, B., et al. 2012, ApJ, 761, 22
 Songaila, A., Cowie, L. L., Hogan, C. J., & Rugers, M. 1994a, Nature, 368, 599
 Songaila, A., Cowie, L. L., Vogt, S., et al. 1994b, Nature, 371, 43
 Srianand, R., Petitjean, P., & Ledoux, C. 2000, Nature, 408, 931
 Srianand, R., Chand, H., Petitjean, P., & Aracil, B. 2004, Phys. Rev. Lett., 92, 121302
 Srianand, R., Noterdaeme, P., Ledoux, C., & Petitjean, P. 2008, A&A, 482, L39
 Sunyaev, R. A., & Zel'dovich, Y. B. 1972, Comments Astrophys. Space Phys., 4, 173
 Thaddeus, P. 1972, ARA&A, 10, 305
 The Dark Energy Survey Collaboration 2005 [arXiv:astro-ph/0510346]
 Tonry, J. L., Stubbs, C. W., Lykke, K. R., et al. 2012, ApJ, 750, 99
 Uzan, J.-P. 2011, Liv. Rev. Rel., 14, 2
 Uzan, J.-P., Aghanim, N., & Mellier, Y. 2004, Phys. Rev. D, 70, 083533
 Zel'dovich, Y. B., & Sunyaev, R. A. 1969, Ap&SS, 4, 301